ZnO-Based Hollow Nanoparticles by Selective Etching: Elimination and Reconstruction of Metal–Semiconductor Interface, Improvement of Blue Emission and Photocatalysis

Haibo Zeng,[†,*] Weiping Cai,[†,*] Peisheng Liu,[†] Xiaoxia Xu,[†] Huijuan Zhou,[‡] Claus Klingshirn,[‡] and Heinz Kalt[‡]

[†]Key Laboratory of Materials Physics, Institute of Solid State Physics, Chinese Academy of Sciences, Hefei 230031, P. R. China, and [‡]Institute of Applied Physics, University of Karlsruhe (TH), D-76128 Karlsruhe, Germany

ABSTRACT A weak acid selective etching strategy was put forward to fabricate oxide-based hollow nanoparticles (HNPs) using core/shell nanostructures of active metal/oxide nanoparticles as sacrificial templates. ZnO-based HNPs, including pure ZnO, Au/ZnO, Pt/ZnO, and Au/Pt/ZnO HNPs with diameter below 50 nm and shell thickness below 6 nm has been first achieved at low temperature. The diameter, thickness, and even sizes of ZnO and noble metal ultrafine crystals of HNPs can be well adjusted by the etching process. Synchronous with the formation of HNPs, the internal metal–semiconductor interfaces can be controllably eliminated (Zn–ZnO) and reconstructed (noble metal–ZnO). Excitingly, such microstructure manipulation has endued them with giant improvements in related performances, including the very strong blue luminescence with enhancement over 3 orders of magnitude for the pure ZnO HNPs and the greatly improved photocatalytic activity for the noble metal/ZnO HNPs. These give them strong potentials in relevant applications, such as blue light emitting devices, environment remediation, drug delivery and release, energy storage and conversion, and sensors. The designed fabrication procedure is simple, feasible, and universal for a series of oxide and noble metal/oxide HNPs with controlled microstructure and improved performances.

KEYWORDS: ZnO · hollow nanoparticles · selective etching · metal–semiconductor interface · luminescence · photocatalysis

Hollow micro- and nanoscale structures have attracted increasing interest because of their specific structures and properties that differ from their solid counterparts, and wide applications in chemistry, biotechnology, and materials science.[1–5] As the most typical one, spherical hollow structures, especially those with small sizes, have remarkable characteristics of high surface–volume ratio and a low density, and hence potential applications in many areas, such as drug-delivery, sensors, batteries, optics, catalysis, and biologic imaging.[6–8] In addition, from a basic aspect, microstructure, such as heterogeneous interfaces inside materials, still plays a very important role in the performances of materials, especially in the small systems such as hollow nanoparticles (HNPs). However, up to now, a detailed understanding of microstructure designing and adjusting is still lacking for the fabrication of HNPs, as well as for the resulting property improvements.

As a greatly attended material with abundant morphologies and wide applications,[9–14] ZnO spherical hollow structures have recently attracted more and more interest. So far, several methods have been used in the fabrication of ZnO spherical hollow structures.[15–22] First, conversion from metallic zinc is the typical method, which had been achieved in ZnO dandelions by a hydrothermal process based on the Kirkendall effect,[15] and in ZnO mesoporous polyhedral cages[16] and urchins[17] by thermal evaporation based on surface oxidation and vaporization/sublimation of zinc droplets. Second, self-assembly is another important method. Mo and coworkers developed the self-assembly of ZnO nanoobjects (nanorod or nanoplatelet) into microscale hollow structures through a hydrothermal process.[18,19] Similar microspheres assembled from nanorods were also reported by Gao and coworkers.[20] In addition, different templates, such as soft droplet[21] and colloidal sphere,[22] were applied to guided surface growth, forming hollow beads[21] or hollow spheres[22] correspondingly.

Although these ZnO spherical hollow structures can be realized in large quantities, they all are of micrometer size, which greatly limits their performances, especially in size- or surface-to-volume ratio-related

*Address correspondence to hbzeng@issp.ac.cn, wpcai@issp.ac.cn.

Received for review May 18, 2008 and accepted June 30, 2008.

Published online July 12, 2008.
10.1021/nn800353q CCC: $40.75

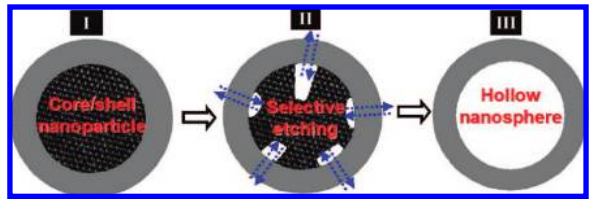

Scheme 1. Illustration of the selective etching strategy for ZnO hollow nanoparticles (HNPs) using a sacrificial template.

fields, such as photocatalysis. On the other hand, the microstructure designing and adjusting are of great significance for their properties from basic considerations, for example, for the controllable construction of metal−semiconductor interfaces in the small and thin HNPs with very high interface density. Usually, metal and semiconductor would form Schottky barriers at their interfaces because of their differences in work function and band alignment, leading to the obvious separation and transfer of photoexcited charges.[23] Such an effect would greatly affect the photoexcited charges' pathway and recombination rate and hence produce significant influence on related properties, such as luminescence and photocatalysis. Unfortunately, up to now, very few reports concentrate on the manipulation of microstructures and properties during the fabrication process of ZnO HNPs.

Herein, we present a simple but effective weak acid selective etching strategy, using Zn/ZnO core/shell nanoparticles (CSNPs)[24−27] as a sacrificial template, to fabricate ZnO hollow nanoparticles (HNPs) with small size, and to *in situ* manipulate their microstructure through controllable elimination or reconstruction of metal−semiconductor interfaces at near room temperature. Excitingly, such microstructure manipulation indeed endues them great improvement in related properties. First, with the elimination of Zn−ZnO interfaces, strong blue luminescence with enhancement over 3 orders of magnitude was achieved in the pure ZnO HNPs. And then, with the one step reconstruction of abundant noble metal−ZnO ultrasmall interfaces, the photocatalytic activity was greatly improved in the noble metal/ZnO HNPs. These achieved small and thin HNPs with special microstructure stride over the known solid nanoparticles or common microscale hollow structure families and potentially, we expect, have applications in optics, catalysis, drug delivery and release, energy storage and conversion, sensors, and advanced optoelectronic devices. In addition, the general strategy involved here can be readily extended to other transition metal oxide systems.

RESULTS AND DISCUSSION

Description of Selective Etching Strategy. The general pathway to fabricate ZnO HNPs is shown in Scheme 1. The Zn/ZnO CSNPs are used as sacrificial template (Scheme 1-I). It is well-known that metals and oxides have different chemical potentials in their reactions with acid, particularly between some active metals and amphoteric oxides. In the weak acid environment, the etching rate of active metal is obviously higher than that of amphoteric oxide.[28] Therefore, when the active metal/oxide CSNPs are immersed in a weak acid solution, the H^+ ions in the solution will diffuse along lattice defects, especially, grain boundaries in the shell layer,[24,26] and enter the core parts, leading to preferential etching of the core parts in addition to weak etching of the shell layer (Scheme1-II). We can use a proper weak acid, such as tartaric acid (TA), to adjust the relative etching rates of active metal in core parts and oxide in shell parts so that the core parts can be preferentially consumed. In this case, with the etching process going on, the core parts could be completely exhausted but the shell parts remain, resulting in the formation of HNPs (Scheme 1-III). Further, if adopting some kinds of weak acids containing noble metal ions as etching agents, such as chloroaurie acid (CA) and chloroplatinic acid (PA), noble metal ions would also diffuse into or through the nanoshell-layers during the etching process, and thus noble metal ultrafine particles (or clusters) could be deposited in the shell-layers of the final HNPs owing to the redox reaction between active and noble metal. We could thus control the components of the nanoshell-layers from pure oxide to noble metal/oxide composites.

As a base, a series of Zn/ZnO core/shell nanoparticles-contained colloidal solutions with average particle diameter below 40 nm depending on laser powers can be obtained by LAL using a zinc target, as previously reported[24−27] (or see the Methods section in detail). Figure 1 gives the typical results with the applied laser power of 70 mJ/pulse. The particles are of 20 nm in average diameter, which are used for a typical sacrificial template. High resolution transmission electron microscopic (HRTEM) examination shows that the particles are of Zn/ZnO core/shell structure, and there are some ultrafine ZnO nanocrystals in the shell-layers and many disordered areas surrounding them. Obviously, the shell layer is a grain boundary-rich system, which favors the following selective etching according to the above strategy. In fact, active metal/oxide nanoparticles are a very common kind of nanoparticle and can be easily obtained by several methods, such as thermal evaporation of zinc.[16,17] This will greatly magnify the universality of this strategy. In addition, another factor for this strategy is the selection of etching agent. Stronger acids, such as nitric acid, were found to disintegrate the template nanoparticles due to the too rapid etching rates on both ZnO shell and Zn core. But weaker acids, such as citric acid, have very slow etching rates and form HNPs with difficulty. The TA, CA, and PA were found to be suitable to form HNPs because of their appropriate etching rates on ZnO shell and Zn core.

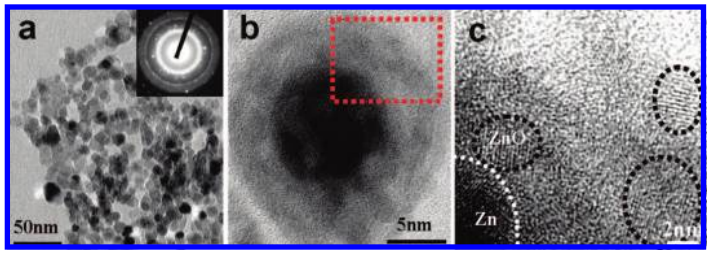

Figure 1. Zn/ZnO core/shell nanoparticles as the sacrificial template.

Characterizations of Weak Acid Etching Process. With the TA etching on the 20 nm Zn/ZnO CSNPs, the nanoparticle composition gradually evolves from two phases Zn/ZnO to single phase ZnO, as shown in X-ray diffraction (XRD) patterns (Figure 2a). The diffraction peaks of both Zn and ZnO decrease with the addition of TA. But Zn diffraction decays much faster than ZnO, and vanishes after dropping sufficient TA. In the complete etching conditions, only the weak ZnO diffraction peaks still exist, indicating that the Zn/ZnO biphase has been gradually transformed to single phase ZnO by the TA etching process. (The incompleteness of the ZnO diffraction peaks in the etched product is due to the high disorder, coinciding with following TEM and electron diffraction characterizations in Figure 4).

Also, the selective etching process can be well demonstrated by the optical absorption spectra evolution (Figure 2b). The deep ultraviolet absorption peak around 250 nm comes from the local surface plasmon resonance (SPR) of metal Zn cores with nanoscale,[24] while the absorption shoulder at 357 nm corresponds to the exciton or interband transition (IBT) absorption of nano-ZnO.[11] With the TA etching process going on, the SPR peak decreases and finally disappears in the complete etching state, while the IBT absorption gradually blue-shifts down to 341 nm, and becomes more dominant in the final spectrum. Such blue-shift, corresponding to remarkable quantum size effect, indicates the thinning of the ZnO shells or reduction in size of the ultrafine ZnO grains in the shells with etching.

Above XRD and optical absorption evolutions have clearly demonstrated the exhaustion of cores and thinning of shells with TA etching process, which are just well coincided with the preferential and weak etching on active metal Zn and amphoteric oxide ZnO by the suitable weak acid, respectively, as presented in the proposed selective etching strategy.

Formation and Control of Pure ZnO HNPs. In addition, with a reduction in the diameter of the template particles, an obvious blue-shift of the optical absorption edges can be observed from the etched products, as shown in Figure 3. On one hand, such a remarkable quantum confinement effect, which had not been observed in the primal template particles, implies that the ZnO shell thickness has been reduced into the quantum size range. On the other hand, there is good consistency between the blue-shift order and the template diameter sequence, demonstrating that the etched products have the same size sequence as their original templates. These results demonstrate that it is feasible for the selective etching strategy not only to fabricate the oxide HNPs with quantum size but also to further control their size through the templates.

Figure 4 shows the TEM images of TA-etched ZnO HNPs from Zn/ZnO templates with different diameters. Obviously, the HNPs have been achieved, and the energy-dispersive X-ray spectroscopy (EDX) and X-ray photoelectron spectra (XPS) reveal the Zn and O compositions, demonstrating the feasibility of the above selective etching strategy. These HNPs are of nearly spherical shape and narrow diameter distribution, as shown in Figure 4a,d,g. Their average diameters are 30.4, 18.6, and 12.6 nm, respectively, exhibiting well-corresponding relations to their templates, which provides a feasible controlling way.

The magnified TEM images (Figure 4b,e,h) present the HNPs more clearly. The selected area electronic diffraction (SAED) patterns of these hollow nanospheres are weak and diffused compared with those of the original nanoparticles, implying the high disorder degree after etching. Moreover, with reduction of the hollow nanosphere in diameter or shell thickness, the SAED patterns evolve from the coexistence of diffraction-ring (including

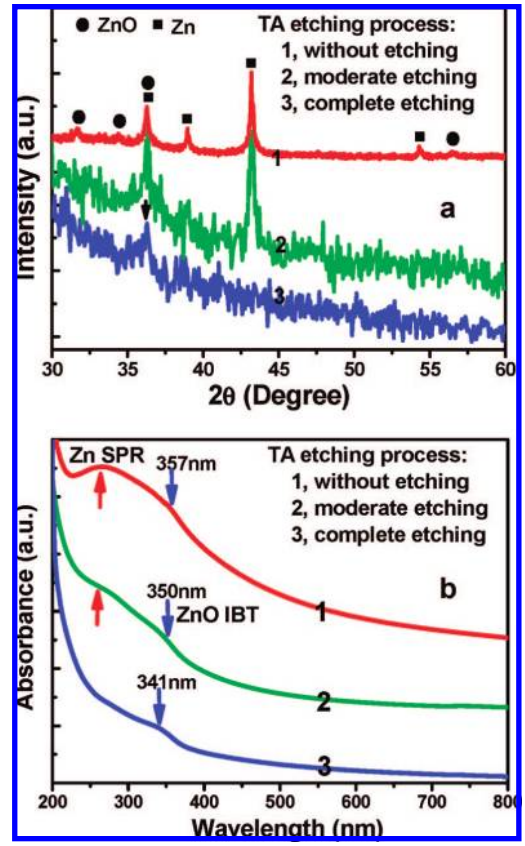

Figure 2. XRD (a) and optical absorption (b) evolutions with the TA etching process.

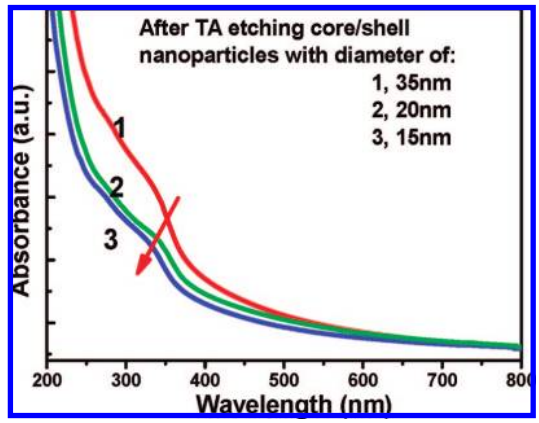

Figure 3. Optical absorption spectra of etched products using template particles with different diameter.

few diffraction dots of ZnO) and amorphous-halation loop (inset in Figure 4d) to the almost completely amorphous-loop (inset in Figure 4f), indicating further decrease of order degree. Such a high disorder feature is in agreement with XRD, SAED, and HRTEM results.

The microstructure of these HNPs is further illuminated in the HRTEM images (Figure 4c,f,i). As a common feature, these ZnO HNPs are of order−disorder microstructure because both ultrafine ZnO crystals and a mass of surrounding disorder area are observed. The clear lattice fringes with 0.26 nm spacing correspond the to (002) planes of wurtzite ZnO. Obviously, such weak acid etching has induced a decrease of the size and number of the ZnO nanocrystals embedded in the shell-layers, in addition to shell thickness or outer-diameter of particles. Especially, the very small HNPs are nearly amorphous. According to the strategy, such high disorder microstructure is induced by the weak etching on the ZnO shell, accompanied by the preferential etching on Zn cores (reaction 1). When the H+ ions diffuse through the primal shell, they also weakly etch the encountered crystal boundaries according to reaction 2 owing to the amphoteric character of ZnO. Reasonably, this will reduce the size of the larger crystals and annihilate the smaller crystals, resulting in the increase of disorder degree. Moreover, the thinner shell

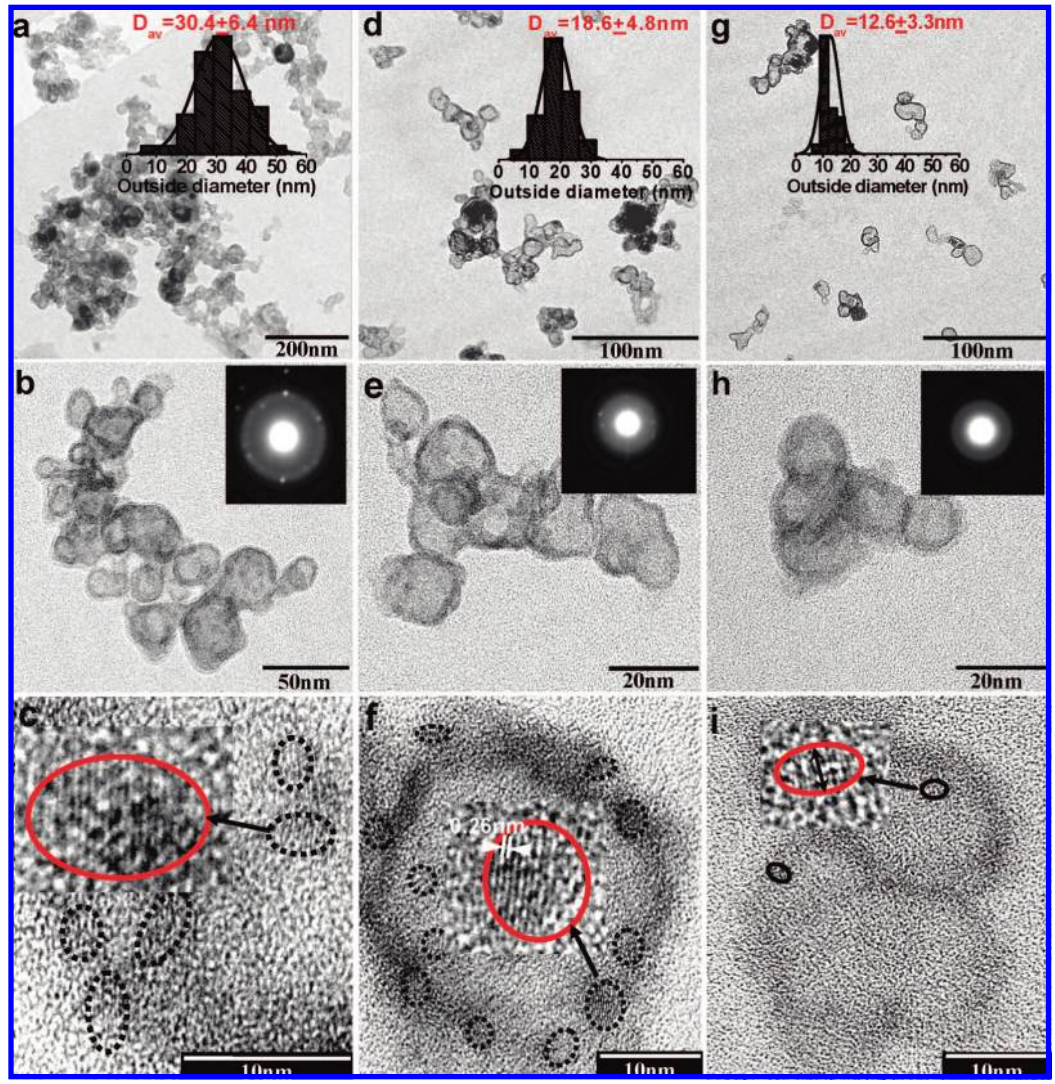

Figure 4. TEM images of ZnO HNPs by CA etching template particles with diameters of 35 (a, b, c), 20 (d, e, f), and 15 nm (g, h, i). The insets show the corresponding diameter distributions and electron diffraction patterns.

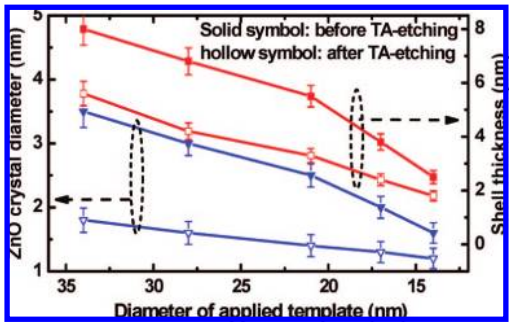

Figure 5. Shell thickness and embedded crystal size of ZnO HNPs *vs* template diameter before and after etching, showing the microstructure controllability.

will favor the selective etching on embedded crystals, and hence the higher disorder degree.

$$Zn + 2H^+ \rightarrow Zn^{2+} + H_2\uparrow \quad (1)$$

$$ZnO + 2H^+ \leftrightarrow Zn^{2+} + H_2O \quad (2)$$

The detailed comparisons of the embedded nanocrystal size and shell thickness between primal templates and etched ZnO HNPs are presented in Figure 5. These two crucial size parameters all decrease after TA etching and further decrease with reduction of template size. Such relativity provides a simple way to control the structure, even the microstructure of ZnO HNPs, by adopting the proper template. The novel microstructure features of the ZnO HNPs can be attributed to the peculiarities of the selective etching strategy. This method is completely different from the conventional unreactive template way, in which the template just guides the surface growth, but not participates in the reaction. Here, the sacrificial templates participate in the reaction with etching agents, which not only results in the formation of HNPs but also greatly affects the microstructure.

Strong Blue Emission of Pure ZnO HNPs. Interestingly, such microstructure change has led to great improvement in the optical properties. Figure 6 presents the room temperature photoluminescence (PL) spectra of the ZnO HNPs under the 370 nm UV excitation. Compared with the weak blue emission of the primal ZnO CSNPs,[24,26,27] these ZnO HNPs exhibit very strong blue emission with enhancement over 3 orders of magnitude. The typical emission band comprises two slightly splitting peaks at 415 and 437 nm, and the intensity is close to the apparatus saturation value (2×10^7). Such blue emissions have relatively narrow full width of half-maximum (fwhm) values of about 70 nm, mainly covering the 400−470 nm blue wave band. Moreover, with the disorder degree increasing, the blue emissions slightly increase. Their high brightness and near homochromatism make them compelling UV-excited phosphors or candidate material for blue light emitting devices. The ZnO HNPs reported here are clearly a viable

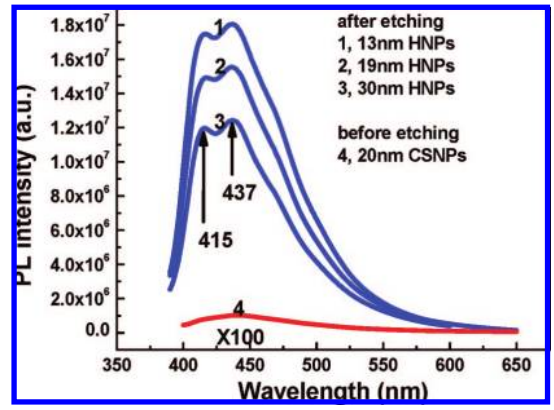

Figure 6. PL spectra of ZnO HNPs with different diameters compared with primal template nanoparticles.

blue light source which can be efficiently and continuously photoexcited by commercially available semiconductor UV emitters.

Except for the familiar UV[29] and green emissions,[30−32] the blue emissions were infrequent and always very weak and broad in previous reports for ZnO.[33−36] The origins of visible luminescence of ZnO have been debated for more than thirty years, especially for the blue emissions because of its sparsity.[30−36] Previously, we suggested that the violet/blue emission be attributed to an interstitial zinc defect level according to its independence in annealing and electron paramagnetic resonance behaviors.[26,27] Here, we focus on the huge enhancement of the blue emission, which should be induced by the great improvement in utilizing the efficiency of the exciting photons in the radiative recombination. Before etching, the Zn−ZnO metal−semiconductor interfaces are abundant in the small ZnO CSNP system, and produce Schottky barriers, inducing the separation and transfer of photoexcited electrons and holes. Thus, the abundant metal−semiconductor interfaces in the primal ZnO CSNPs greatly reduce the radiative recombination efficiency. Moreover, before etching, the ZnO CSNPs have an intense absorption in the UV region, including the excitation light, due to the plasma resonance of nanoscale Zn cores (but only ZnO exciton and band electron absorption after etching),[24] as shown in Figure 7. After etching, the elimination of metal-semiconductor interfaces dispels the charge-separating and excitation-absorbing effects, and hence results in the great enhancement of blue emission. Moreover, the improved disorder by the selective etching would greatly enhance energy transfer from the band edge to the defect states responsible for blue emission, resulting in the blurry band edge emission and much brighter blue emission.

Characterizations of Noble Metal Acid Etching Process. Alternatively, if the Zn/ZnO template nanoparticles are etched by weak acid-containing noble metal ions, we can get the ZnO HNPs embedded with ultrafine noble

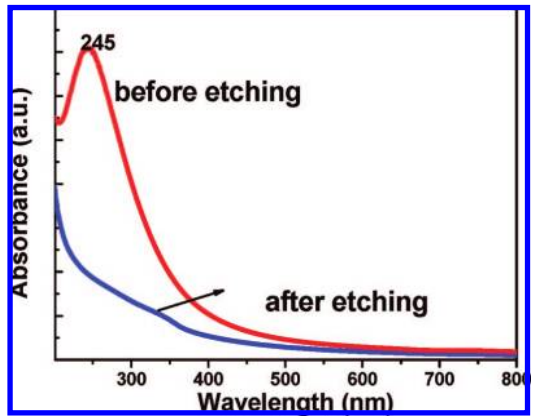

Figure 7. Optical absorption spectra of ZnO HNPs and primal nanoparticles.

metal particles in the shell layer. Similarly, the CA ($HAuCl_4$) etching process can also be well traced by the optical absorption spectra evolution, as illustrated in Figure 8. With the etching going on, the Zn SPR absorption peak gradually decreases till disappearance, accompanied by the blue-shift of the ZnO IBT absorption shoulder. These phenomena are similar to those in the TA etching process, indicating the etching-induced exhaustion of the Zn cores and thinning of the ZnO shells as described in the proposed strategy. What is different and should be noticed here is that a new absorption peak around 550 nm gradually appears and strengthens, which originates from the SPR of Au nanoparticles. These results imply that the CA etching not only leads to the transformation of ZnO HNPs from sacrificial templates, but also forms the Au nanoparticles at the same time, which could have incorporated into the final ZnO matrix in the form of Au/ZnO HNPs.

Formation and Control of Noble Metal/ZnO HNPs. Figure 9 presents the CA etching results. Assuredly, the Au/ZnO HNPs have been formed. From the TEM image (Figure 9a), it can be seen that the small Au nanoparticles are well dispersed and attached in the HNPs (solid and dashed arrow point out ZnO and Au, respectively). No separated or aggregated Au particles are found beyond the hollow nanospheres. From the size statistic, the average diameter of Au nanoparticles is as small as 3 nm, and that of the HNPs is without obvious difference from the used templates. The EDX in Figure 9b demonstrates the Au, Zn, and O composition in the area of HNPs. All these results are in good agreement to the above ABS features, including composition and size changing. The microstructure is further revealed by the HRTEM image in Figure 9c. The plane spaces of the framework and in the embedded nanoparticle are 0.26 and 0.23 nm, just corresponding to the ZnO (002) planes and the Au (111) planes, respectively. Contrasted to the TA-etched HNPs, the ZnO framework in the CA-etched HNPs is of higher crystalline quality, which can be attributed to the weaker etching on ZnO shell layers and on the embedded ZnO ultrafine crystals.

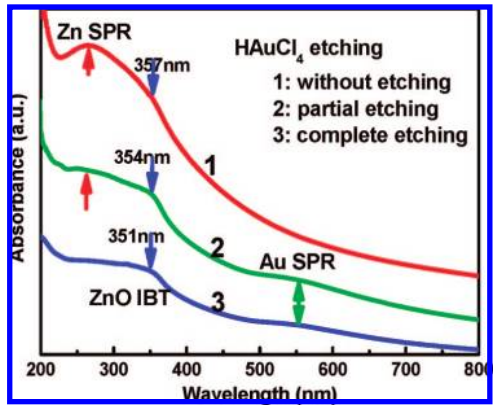

Figure 8. Optical absorption evolutions with the CA etching process.

Similarly, the PA (H_2PtCl_6) etching can induce the formation of Pt/ZnO HNPs, as shown in Figure 10. The HNP morphology and Pt composition are well demonstrated by the TEM image (Figure 10a) and EDX spectrum (Figure 10b), respectively. It can be believed that Pt has been successfully inserted into the ZnO HNP during the etching process because no separated Pt small particles are found. From the HRTEM image in Figure 10c, the Pt clusters with high contrast due to their higher electron density than ZnO matrix can be easily seen in a large quantity. At the same time, the ZnO shell frame is found to be well crystalline from their clear lattice fringes.

Further, as an extension of above noble metal acid etching, the multinoble metal/ZnO HNPs can be easily obtained by the corresponding multistep etching process. Typically, the Au/Pt/ZnO HNPs were fabricated by CA-PA etching (first $HAuCl_4$ and then H_2PtCl_6), as shown in Figure 11. The TEM image (Figure 11a) demonstrates the HNP morphology without difference from the above single metal/ZnO HNPs. The EDX (Figure 11b) reveals the Au and Pt composition. The HRTEM image (Figure 11c) clearly shows the noble metal nanoparticles with a diameter below 3 nm and higher contrast than the ZnO matrix. These observations confirm the coexistence of Au and Pt ultrafine particles in the HNPs.

When the Zn/ZnO templates are etched by weak acid-containing noble metal ions, the larger chemical potential difference between noble metal ions and Zn cores will lead to the replacing reaction to be dominant as equation 3, compared with relatively weak reactions 1 and 2. The obtained results imply that three events, including ions' diffusion, redox reaction (mainly equation 3), and *in situ* deposition of a noble metal arise almost synchronously in the pathway during the etching process. The synchronous reaction-diffusion behavior of noble metal ions in this report is, to some extent, similar to the nanoscale Kirkendall effect,[37–40] in which the material density gradient leads to the two-way diffusion in the reaction process, typically for an example of $ZnAl_2O_4$ nanotubes formed by solid phase reaction and two-way diffusion of $ZnO-Al_2O_3$.[38,39] The similar

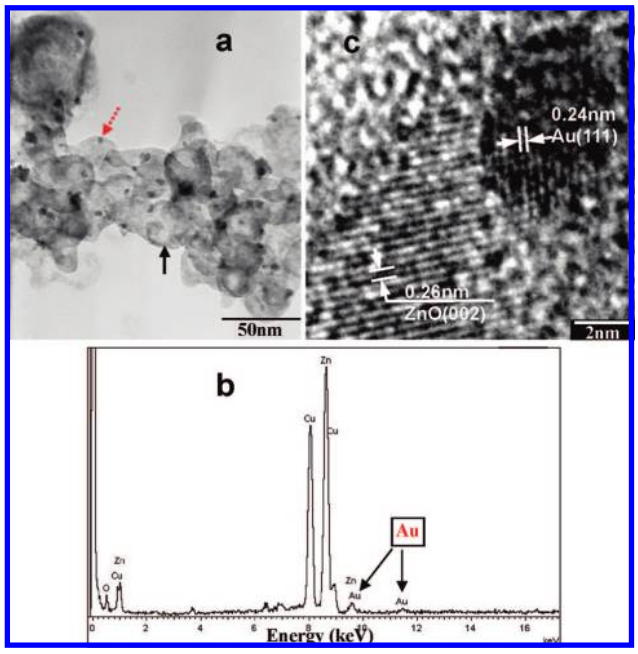

Figure 9. TEM image (a), EDX spectrum (b), and HRTEM image (c) of Au/ZnO HNPs by CA etching.

two-way diffusion would take place during the reaction of Zn and noble metal ions, resulting in the hollowing of the cores and incorporation of noble metal clusters in the shells.

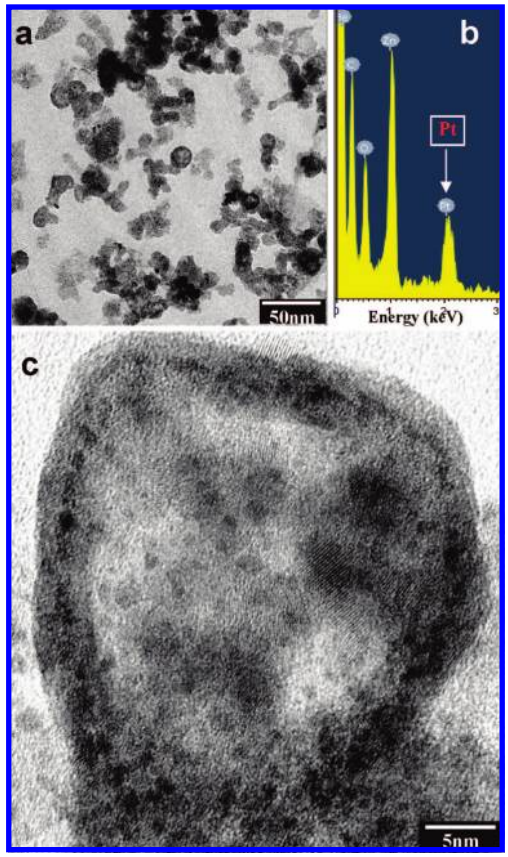

Figure 10. TEM image (a), EDX spectrum (b), and HRTEM image (c) of Pt/ZnO HNPs by PA etching.

$$nZn + 2M^{n+} \rightarrow nZn^{2+} + 2M^{0},\ (M = \text{Pt, Au, Ag, Pd}) \quad (3)$$

These results have demonstrated that the proposed selective etching strategy is also suitable to fabricate noble metal ultrafine particles−embedded oxide HNPs, exhibiting good universality and controllability in the components. More importantly, considering the small size and high density of these noble metal clusters, without doubt, a great amout of metal−semiconductor interfaces have been reconstructed, forming abundant Schottky barriers in the HNPs. These could endue the noble metal/semiconductor HNPs with strong separation ability for the photogenerated charges.[40–42] Moreover, the embedding state, rather than usual surface attaching state, will improve the effective interfaces and further favor such ability. Thus, these noble metal/oxide HNPs could perform remarkably in charge-separating favored fields, such as photocatalysis.

Improved Photocatalysis of Noble Metal/ZnO HNPs. The photocatalysis efficiencies of the typical HNPs in degradation of methyl orange (MO) were presented in Figure 12, compared with conventional TiO_2 reference sample (P25). For the pure ZnO HNPs, very poor photodegradation ability can be seen. However, for the Pt/ZnO HNPs, the methyl orange can be degraded about

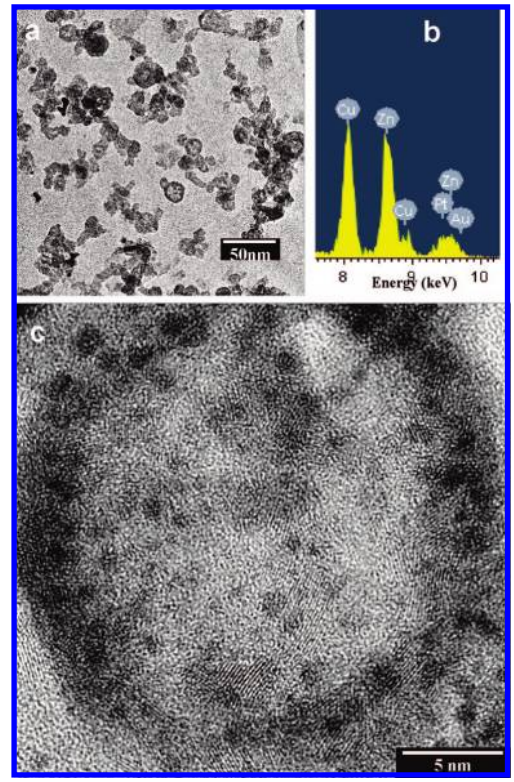

Figure 11. TEM image (a), EDX spectrum (b), and HRTEM image (c) of Au/Pt/ZnO HNPs by CA-PA etching.

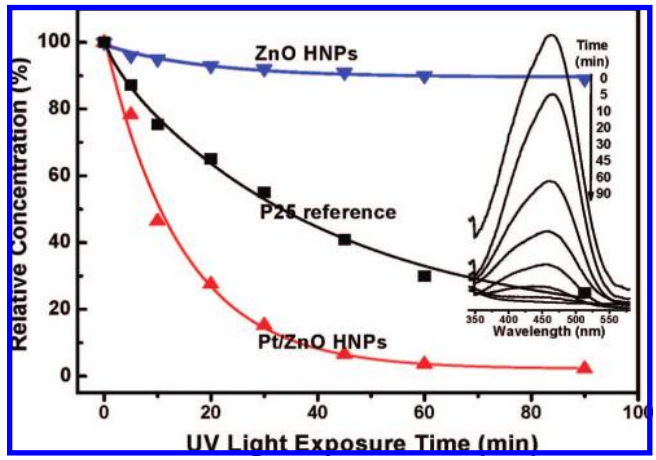

Figure 12. MO photodegradation rate of pure ZnO and Pt/ZnO HNPs, compared with reference P25 powder.

90% in 40 min in our experimental conditions (the Au/ZnO and Au/Pt/ZnO HNPs are similarly effective), which is faster than that of P25 reference. Such improvement can be attributed to the several outstanding features of the Pt/ZnO HNPs, including the small size of the noble metal clusters and ZnO shell thickness, high surface-volume ratio, and effective electron−hole separation of the Schottky barriers.[41–43] Also, the whole surface-contact of embedded noble metal ultrafine particles to the ZnO matrix takes an important role, adequately playing the function of metal-semiconductor heterojunctions, facilitating the charge transfer, and hence improving the photocatalysis efficiency.

One of the biggest problems for the photocatalysis of ZnO is its photostability, which is related with the crystallinity, the charge transfer, and others. Therefore, to be a good photocatalyst, it has to be stable and reusable. Since in the noble metal/semiconductor system metal acts as a reservoir for electrons, holes will conduct to the surface of semiconductors as the oxidant to oxidize the organic dyes. Electrons at the surface can reduce Zn^{2+} to Zn, namely, photocorrosion of ZnO. But for the noble metal/ZnO case, electrons are confined in the metal part, and then the photocorrosion should be depressed.

The great improvement in photocatalysis efficiency of Pt/ZnO to pure ZnO HNPs could also be attributed to their photostability. The TEM observations on the remaining powders after the photocatalytic reactions are used to investigate their photostability. The results are shown in Figure 13. Obviously, the pure ZnO HNPs has been disintegrated into ultrafine nanoparticles, as shown in Figure 13a. Such a phenomenon is induced by the photocorrosion effect of ZnO: that the photogenerated charges react not only with polymer molecules but also ZnO itself, leading to the dissolution of the ZnO framework. The high disorder degree greatly favors the photocorrosion effect, resulting in low photocatalysis efficiency. However, the ZnO framework in Pt/ZnO HNPs is of high crystallinity, thus the photocorrosion effect should be minor. Indeed, the TEM image in Figure 13b demonstrates that there is almost no obvious change in the morphology of the Pt/ZnO HNPs after the photocatalysis reaction. Therefore, the sacrificial-template selective-etching strategy has opened a simple, effective, and low cost process for the fabrication of noble metal−semiconductor interface-abundant photocatalysts, and has considerable universality, such as extending into noble metal/TiO_2 syestems.

CONCLUSIONS AND REMARKS

In summary, a metal/oxide sacrificial template-selective etching strategy was put forward to fabricate pure oxide and noble metal/oxide small and thin HNPs at low temperature. The architecture of ZnO, Au/ZnO, Pt/ZnO, and Au/Pt/ZnO HNPs with a diameter below 50 nm and thickness below 6 nm was successfully achieved and well controlled. Importantly, with the formation of these HNPs, the metal-semiconductor interfaces were controllably eliminated (Zn−ZnO) and reconstructed (noble metal−ZnO) inside the materials. The elimination of Zn cores in pure ZnO HNPs is mainly attributed to the preferential etching of the weak acid, but the selective etching on the ZnO shells resulted in the high disorder degree. The noble metal clusters incorporation in HNPs was induced by the diffusion-redox-precipitation process during the reaction of Zn cores with noble metal ions. Excitingly, such microstructure manipulation has endued them great enhancements in related performances. The strong blue luminescence with enhancement over 3 orders of magnitude was caused by the elimination of the charge-separating metal-semiconductor interfaces, excitation-absorbing of Zn cores, and disorder-enhanced energy transfer from the band edge to

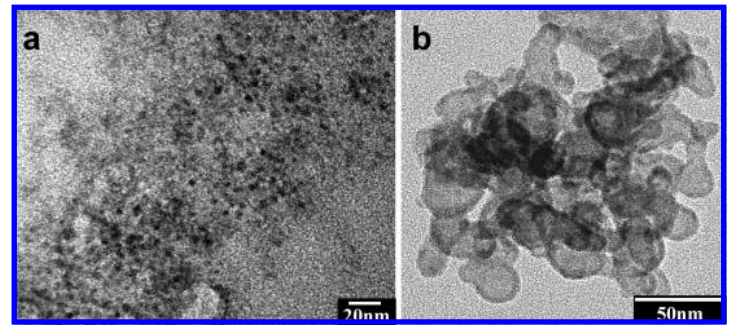

Figure 13. TEM images of remainders after the photocatalysis reaction using pure ZnO (a) and Pt/ZnO (b) HNPs.

the defect states. And then, the photocatalytic activity was greatly improved for the noble metal/ZnO HNPs because of the more effective electron−hole separation induced by the reconstructed abundant metal−semiconductor interfaces, the whole-surface contact between Pt clusters and ZnO matrix, and the resulting huge specific surface area of the hollow and ultrathin shell structure.

These produced HNPs with special microstructure properties over the known solid nanoparticles or common microscale hollow structure families and potentially, we expect, have applications in optics, catalysis, drug delivery and release, energy storage and conversion, sensors, and advanced optoelectronic devices. The general strategy involved here can be readily extended to other transition-metal oxide systems, for example, TiO_2 and SnO_2 HNPs, the noble metal (Pt, Pd, Au, Ag) incorporation, and even multioxide HNPs. So, this strategy may be a convenient and effective and universal bridge toward the mono- or multicomponent hollow nanospheres with designed interfaces and improved properties.

METHODS

The Zn/ZnO core/shell nanoparticle colloids were synthesized by laser ablation in liquid (LAL) as previously reported.[24−27] Briefly, a zinc plate (99.99%) was fixed on a bracket in a glass vessel filled with 10 mL of 0.05 M sodium dodecyl sulfate (SDS, 99.5%) aqueous solution. The plate was ablated (irradiated) for 30 min by the first harmonic of Nd:YAG laser (1064 nm, frequency 10 Hz, pulse duration 10 ns) with 2 mm focused spot. The applied laser power was adjusted from 35 to 100 mJ/pluse. The 50 mL obtained colloidal solutions were etched by weak acid aqueous solutions: tartaric acid (TA, $C_4H_6O_6$, 10 mM, 20 mL), chloroaurie acid (CA, $HAuCl_4$, 2 mM, 10 mL), and chloroplatinic acid (PA, H_2PtCl_6, 2 mM, 10 mL), respectively. The etching agents (one kind, or first one and then another kind) were slowly added into the colloidal solution droplet by droplet, while the solution was continually stirred and kept at an invariable temperature of 40 °C by a stirrer with a heating pedestal. After etching, the colloidal solutions were centrifuged at 14000 rpm and then ultrasonically redispersed in ethanol for more than five cycles to remove the surfactants, and finally draft-dried in oven at 40 °C for 24 h.

The obtained powder samples were characterized by powder X-ray diffraction (XRD, Philips X'Pert with Cu Kα line of 0.15419 nm), transmission electron microscopy (TEM, JEM-200CX; HRTEM, JEOL-2010), and energy dispersive X-ray spectrum (EDX). The optical absorption spectra were recorded by a Cary 5E UV−vis−IR spectrometer for the obtained colloidal solutions. The photoluminescence (PL) spectra were measured at Edinburgh luminescence spectrometer (FLS 920) with Xe lamp excitation. The photocatalytic performance was evaluated by monitoring the optical absorption peak of methyl orange at 465 nm. Different catalyst powders (10 mg) (ZnO, Au/ZnO, Pt/ZnO, Pt/Au/ZnO) were added into 10^{-5} M (20 mL) methyl orange aqueous solution and vigorously stirred for 30 min, and then the mixed solution was irradiated by a ultraviolet lamp with a power of 125 W and center wavelength of 365 nm. Solutions of about 1 mL were taken out after different irradiation times for optical absorption measurements.

Acknowledgment. This work was financially supported by NSFC (Grant No. 10604055 and 50671100), the National Basic Research Program of China (Grant No 2007CB936604), and the Knowledge Innovation Program of the Chinese Academy of Sciences (Grant No. KJCX2-SW-W31).

REFERENCES AND NOTES

1. Gao, Y. H.; Bando, Y. Carbon Nanothermometer Containing Gallium-Gallium's Macroscopic Properties are Retained on a Miniature Scale in this Nanodevice. *Nature* **2002**, *415*, 599.
2. Shen, G. Z.; Bando, Y.; Ye, C. H.; Yuan, X. L.; Sekiguchi, T.; Golberg, D. Single-Crystal Nanotubes of II-V Semiconductors. *Angew. Chem., Int. Ed.* **2006**, *45*, 7568–7572.
3. Ye, C. H.; Bando, Y.; Shen, G. Z.; Golberg, D. Formation of Crystalline $SrAl_2O_4$ Nanotubes by a Roll-Up and Post-Annealing Approach. *Angew. Chem., Int. Ed.* **2006**, *45*, 4922–4926.
4. Mathiowitz, E.; Jacob, J. S.; Jong, Y. S.; Carino, G. P.; Chickering, D. E.; Chaturvedi, P.; Santos, C. A.; Vijayaraghavan, K.; Montgomery, S.; Bassett, M. Biologically Erodable Microsphere as Potential Oral Drug Delivery System. *Nature* **1997**, *386*, 410–414.
5. Yamada, T.; Iwasaki, Y.; Tada, H.; Iwabuki, H.; Chuah, M. K. L.; VandenDriessche, T.; Fukuda, H.; Kondo, A.; Ueda, M.; Seno, M. Nanoparticles for the Delivery of Genes and Drugs to Human Hepatocytes. *Nat. Biotechnol.* **2003**, *21*, 885–890.
6. Suh, W. H.; Jang, A. R.; Suh, Y. H.; Suslick, K. S. Porous, Hollow, and Ball-in-ball Metal Oxide Microspheres: Preparation, Endocytosis, and Cytotoxicity. *Adv. Mater.* **2006**, *18*, 1832–1837.
7. Chen, J.; Saeki, F.; Wiley, B. J.; Cang, H.; Cobb, M. J.; Li, Z. Y.; Au, L.; Zhang, H.; Kimmey, M. B.; Li, X.; Nan, D. Gold Nanocages: Bioconjugation and Their Potential Use as Optical Imaging Contrast Agents. *Nano. Lett.* **2005**, *5*, 473–477.
8. Su, C. H.; Sheu, H. S.; Lin, C. Y.; Huang, C. C.; Lo, Y. W.; Pu, Y. C.; Weng, J. C.; Shieh, D. B.; Chen, J. H.; Yeh, C. S. Nanoshell Magnetic Resonance Imaging Contrast Agents. *J. Am. Chem. Soc.* **2007**, *129*, 2139–2146.
9. Qin, Y.; Wang, X. D.; Wang, Z. L. Microfibre-Nanowire Hybrid Structure for Energy Scavenging. *Nature* **2008**, *451*, 809–813.
10. Ju, S.; Facchetti, A.; Xuan, Y.; Liu, J.; Ishikawa, F.; Ye, P. D.; Zhou, C. W.; Marks, T. J.; Janes, D. B. Fabrication of Fully Transparent Nanowire Transistors for Transparent and Flexible Electronics. *Nat. Biotechnol.* **2007**, *2*, 378–384.
11. Huang, M. H.; Mao, S.; Feick, H.; Yan, H. Q.; Wu, Y. Y.; Kind, H.; Weber, E.; Russo, R.; Yang, P. D. Room-Temperature Ultraviolet Nnanowire Nanolasers. *Science* **2001**, *292*, 1897–1899.
12. Pacholski, C.; Kornowski, A.; Weller, H. Self-Assembly of ZnO: From Nanodots, to Nanorods. *Angew. Chem., Int. Ed.* **2002**, *41*, 1188–1191.
13. Park, W. I.; Yi, G. C. Electroluminescence in *n*-ZnO Nanorod Arrays Vertically Grown on p-GaN. *Adv. Mater.* **2004**, *16*, 87–90.
14. Shen, G. Z.; Bando, Y.; Liu, B. D.; Golberg, D.; Lee, C. J. Characterization and Ffield-Emission Properties of Vertically Aligned ZnO Nanonails and Nanopencils Fabricated by a Modified Thermal-Evaporation Process. *Adv. Funct. Mater.* **2006**, *16*, 410–416.
15. Liu, B.; Zeng, H. C. Fabrication of ZnO "Dandelions" *via* a Modified Kirkendall Process. *J. Am. Chem. Soc.* **2004**, *126*, 16744–16746.
16. Gao, P. X.; Wang, Z. L. Mesoporous Polyhedral Cages and Shells Formed by Textured Self-Assembly of ZnO Nanocrystals. *J. Am. Chem. Soc.* **2003**, *125*, 11299–11305.
17. Shen, G. Z.; Bando, Y.; Lee, C. J. Synthesis and Evolution of Novel Hollow ZnO Urchins by a Simple Thermal

Evaporation Process. *J. Phys. Chem. B* **2005**, *109*, 10578–10583.
18. Mo, M.; Yu, J. C.; Zhang, L. Z.; Li, S. K. A. Self-Assembly of ZnO Nanorods and Nanosheets into Hollow Microhemispheres and Microspheres. *Adv. Mater.* **2005**, *17*, 756–760.
19. Mo, M. S.; Lim, S. H.; Mai, Y. W.; Zheng, R. K.; Ringer, S. P. *In Situ* Self-Assembly of Thin ZnO Nanoplatelets into Hierarchical Mesocrystal Microtubules with Surface Grafting of Nanorods: A General Strategy Towards Hollow Mesocrystal Structures. *Adv. Mater.* **2008**, *20*, 339–342.
20. Gao, S. Y.; Zhang, H. J.; Wang, X. M.; Deng, R. P.; Sun, D. H.; Zheng, G. L. ZnO-Based Hollow Microspheres: Biopolymer-Assisted Assemblies from ZnO Nanorods. *J. Phys. Chem. B* **2006**, *110*, 15847–15852.
21. Jiang, Z. Y.; Xie, Z. X.; Zhang, X. H.; Lin, S. C.; Xu, T.; Xie, S. Y.; Huang, R. B.; Zheng, L. S. Synthesis of Single-Crystalline ZnO Polyhedral Submicrometer-Sized Hollow Beads Using Laser-Assisted Growth with Ethanol Droplets as Soft Templates. *Adv. Mater.* **2004**, *16*, 904–907.
22. Wang, X.; Hu, P.; Yuan, F. L.; Yu, L. J. Preparation and Characterization of ZnO Hollow Spheres and ZnO-Carbon Composite Materials Using Colloidal Carbon Spheres as Templates. *J. Phys. Chem. C* **2007**, *111*, 6706–6712.
23. Linsebigler, A. L.; Lu, G. Q.; Yates, J. T. Photocatalysis on TiO_2 Surfaces - Principles, Mechanisms, and Selected Results. *Chem. Rev.* **1995**, *95*, 735–758.
24. Zeng, H. B.; Cai, W. P.; Li, Y.; Hu, J. L.; Liu, P. S. Composition/Structural Evolution and Optical Properties of ZnO/Zn Nanoparticles by Laser Ablation in Liquid Media. *J. Phys. Chem. B* **2005**, *109*, 18260–18266.
25. Zeng, H. B.; Cai, W. P.; Cao, B. Q.; Hu, J. L.; Li, Y.; Liu, P. S. Surface Optical Phonon Raman Scattering in Zn/ZnO Core-Shell Structured Nanoparticles. *Appl. Phys. Lett.* **2006**, *88*, 181905–181908.
26. Zeng, H. B.; Li, Z.; Cai, W. P.; Cao, B.; Liu, P.; Yang, S. Microstructure Control of Zn/ZnO Core/Shell Nanoparticles and Their Temperature-Dependent Blue Emissions. *J. Phys. Chem. B* **2007**, *111*, 14311–14317.
27. Zeng, H. B.; Cai, W. P.; Hu, J. L.; Duan, G. T.; Liu, P. S.; Li, Y. Violet Photoluminescence from Shell Layer of Zn/ZnO Core-Shell Nanoparticles Induced by Laser Ablation. *Appl. Phys. Lett.* **2006**, *88*, 171910–171912.
28. Jiang, Q.; Wu, Z. Y.; Wang, Y. M.; Cao, Y.; Zhou, C. F.; Zhu, J. H. Fabrication of Photoluminescent ZnO/SBA-15 through Directly Dispersing Zinc Nitrate into the As-Prepared Mesoporous Silica Occluded with Template. *J. Mater. Chem.* **2006**, *16*, 1536–1542.
29. Meyer, B. K.; Alves, H.; Hofmann, D. M.; Kriegseis, W.; Forster, D.; Bertram, F.; Christen, J.; Hoffmann, A.; Strassburg, M.; Dworzak, M. Bound Exciton and Donor-Acceptor Pair Recombinations in ZnO. *Phys. Status Solidi B* **2004**, *241*, 231–260.
30. Vanheusden, K.; Seager, C. H.; Warren, W. L.; Tallant, D. R.; Voigt, J. A. Correlation Between Photoluminescence and Oxygen Vacancies in ZnO Phosphors. *Appl. Phys. Lett.* **1996**, *68*, 403–405.
31. Lin, B. X.; Fu, Z. X.; Jia, Y. B. Green Luminescent Center in Undoped Zinc Oxide Films Deposited on Silicon Substrates. *Appl. Phys. Lett.* **2001**, *79*, 943–945.
32. Tam, K. H.; Cheung, C. K.; Leung, Y. H.; Djurisic, A. B.; Ling, C. C.; Beling, C. D.; Fung, S.; Kwok, W. M.; Chan, W. K.; Phillips, D. L. Defects in ZnO Nanorods Prepared by a Hydrothermal Method. *J. Phys. Chem. B* **2006**, *110*, 20865–20871.
33. Bylander, E. G. Surface Effects on the Low-Energy Cathodoluminescence of Zinc Oxide. *J. Appl. Phys.* **1978**, *49*, 1188–1195.
34. Wu, J. J.; Liu, S. C. Low-Temperature Growth of Well-Aligned ZnO Nanorods by Chemical Vapor Deposition. *Adv. Mater.* **2002**, *14*, 215–218.
35. Zhang, W. H.; Shi, J. L.; Wang, L. Z.; Yan, D. S. Preparation and Characterization of ZnO Clusters inside Mesoporous Silica. *Chem. Mater.* **2000**, *12*, 1408–1413.
36. Guo, L.; Yang, S. H.; Yang, C. L.; Yu, P.; Wang, J. N.; Ge, W. K.; Wong, G. K. L. Synthesis and Characterization of Poly(vinylpyrrolidone)-Modified Zinc Oxide Nanoparticles. *Chem. Mater.* **2000**, *12*, 2268–2274.
37. Yin, Y. D.; Rioux, R. M.; Erdonmez, C. K.; Hughes, S.; Somorjai, G. A.; Alivisatos, A. P. Formation of Hollow Nanocrystals through the Nanoscale Kirkendall Effect. *Science* **2004**, *304*, 711–714.
38. Fan, H. J.; Knez, M.; Scholz, R.; Nielsch, K.; Pippel, E.; Hesse, D.; Zacharias, M.; Gosele, U. Monocrystalline Spinel Nanotube Fabrication Based on the Kirkendall Effect. *Nat. Mater.* **2006**, *5*, 627–631.
39. Fan, H. J.; Knez, M.; Scholz, R.; Hesse, D.; Nielsch, K.; Zacharias, M.; Gosele, U. Influence of Surface Diffusion on the Formation of Hollow Nanostructures Induced by the Kirkendall Effect: The Basic Concept. *Nano. Lett.* **2007**, *7*, 993–997.
40. Fan, H. J.; Gosele, U; Zacharias, M. Formation of Nanotubes and Hollow Nanoparticles Based on Kirkendall and Diffusion Processes: A Review. *Small* **2007**, *3*, 1660–1671.
41. Height, M. J.; Pratsinis, S. E.; Mekasuwandumrong, O.; Praserthdam, P. Ag-ZnO Catalysts for UV-Photodegradation of Methylene Blue. *Appl. Catal. B: Environ.* **2006**, *63*, 305–312.
42. Wu, J. J.; Tseng, C. H. Photocatalytic Properties of Nc-Au/ZnO Nanorod Composites. *Appl. Catal. B* **2006**, *66*, 51–57.
43. Ammari, F.; Lamotte, J.; Touroude, R. An Emergent Catalytic Mmaterial: Pt/ZnO Catalyst for Selective Hydrogenation of Crotonaldehyde. *J. Catal.* **2004**, *221*, 32–42.